




Article

Development and Optimization of a Micro-Baffle for the Enhancement of Heat Transfer in Film Boiling

Onur Muhammed Sarikaya ¹, Mustafa Kuzay ¹, Sibel Yilmaz ¹ and Ender Demirel ^{1,2,*}

¹ Design and Simulation Technologies Inc., 26480 Eskisehir, Türkiye; omsarikaya@dstechs.net (O.M.S.); mkuzay@dstechs.net (M.K.); sibelyilmaz@dstechs.net (S.Y.)

² Department of Civil Engineering, Eskisehir Osmangazi University, 26040 Eskisehir, Türkiye

* Correspondence: edemirel@dstechs.net

Abstract: This study represents the development and optimization of a micro-baffle design to enhance heat transfer in film boiling. Numerical simulations are performed using an open-source computational fluid dynamics (CFD) model, which incorporates the Lee model for momentum source associated with the phase change, and the Volume of Fluid (VOF) method to capture bubble dynamics. A comparison of the numerical results with the previous numerical and experimental data confirmed the validity of the numerical model. The influence of key design parameters was systematically investigated. The results revealed that a vertical baffle provided the maximum performance. The optimal baffle design achieved a 57.4% improvement in the Nusselt number and a 66.4% increase in critical heat flux (CHF). Furthermore, the proposed design facilitated continuous bubble formation, even with a reduced temperature difference between the heated surface and the subcooled liquid, which is crucial for energy-efficient thermal management in engineering systems. Ultimately, this study demonstrates the potential of micro-baffle designs in controlling bubble dynamics and improving heat transfer in film boiling, thereby aiding the design of efficient thermal systems.

Keywords: film boiling; heat transfer enhancement; micro-baffle design; CFD; bubble dynamics



Citation: Sarikaya, O.M.; Kuzay, M.; Yilmaz, S.; Demirel, E. Development and Optimization of a Micro-Baffle for the Enhancement of Heat Transfer in Film Boiling. *Energies* **2024**, *17*, 5224. <https://doi.org/10.3390/en17205224>

Academic Editor: Frede Blaabjerg

Received: 3 September 2024

Revised: 2 October 2024

Accepted: 14 October 2024

Published: 21 October 2024



Copyright: © 2024 by the authors. Licensee MDPI, Basel, Switzerland. This article is an open access article distributed under the terms and conditions of the Creative Commons Attribution (CC BY) license (<https://creativecommons.org/licenses/by/4.0/>).

1. Introduction

Film boiling is of great importance in both industrial and scientific applications due to its distinct thermal features such as high heat flux, a significant temperature difference between the heated surface and the boiling liquid, and the formation of a stable vapor film that insulates the surface. Accurate modeling of film boiling is essential for predicting the performance of emergency core cooling systems and ensuring reactor safety in the nuclear industry [1]. Film boiling also plays a vital role in the storage and transfer of cryogenic liquids such as nitrogen and hydrogen. Understanding the heat transfer mechanism is essential for designing efficient insulation and heat transfer to minimize evaporation losses in these applications [2]. Quenching processes in the metallurgical industry have emerged as another application area of film boiling. As the hot metal is immersed in a coolant, film boiling occurs initially, followed by a transition to nucleate boiling. Controlling the transition between these boiling regimes is essential for achieving the desired mechanical properties in metals [3]. Film boiling is widely utilized in spacecraft thermal management systems because spacecraft often experience extreme temperature variations and film boiling can be used to manage heat transfer during re-entry or in cryogenic fuel tanks [4]. Therefore, managing film boiling has attracted significant interest in various engineering applications in recent years.

Researchers have developed various approaches such as the addition of surfactants, surface coatings, contact crossflow packed beds, multi-stage flash, fluidized beds, and geometric modifications to enhance heat transfer in film boiling. Surfactants enhance

heat transfer by reducing surface tension, leading to smaller bubble diameters and more frequent bubble formation, therefore increasing heat transfer during the boiling process. You et al. [5] achieved a significant increase in the Critical Heat Flux (CHF) value using the Al_2O_3 . Park et al. [6] demonstrated that the addition of graphene nanofluids could result in an 84% increase in the CHF. Adding specific patterns and geometries to the surface is crucial for controlling the formation of vapor bubbles and improving the heat transfer during boiling. Additionally, the potential benefits of increasing surface area and geometry make these approaches viable in terms of heat transfer performance because these modifications enhance nucleation sites, promote more efficient fluid distribution, and reduce thermal resistance. They can significantly improve the overall heat transfer rate by facilitating faster bubble detachment and increasing the surface area of heat exchange. Mori and Okuyama et al. [7] investigated the influence of honeycomb structures on heat transfer performance and demonstrated that the proposed honeycomb could increase the CHF by two-point-five times compared to that of a flat plate. The use of a porous fence plate in subcooled flow boiling experiments resulted in a 2.3-fold increase in heat transfer performance [8]. This improvement was observed at a specific pitch-to-diameter ratio of 2.5:1.7. On the other hand, Hao et al. [9] investigated the effect of a deformable structure made from shape memory alloy with working fluids such as ethanol, FC-72, and water. A significant increase was achieved in the Heat Transfer Coefficient (HTC) and the adaptive control of boiling heat transfer could be attained using these structures. Surface coatings can modify the energy distribution across a surface, thereby altering vapor bubble formation and enhancing their detachment, due to advantages such as ease of application and the ability to control surface properties. However, the wear of the coating material over time and its inherent thermal resistance can limit their applications. Surtaev et al. [10] studied capillary porous coating to enhance heat transfer in pool boiling. They found that the capillary-porous coating, applied by the plasma spraying method, had a porosity of 60% with a variable thickness of 400–1390 μm . The coating process increased the heat transfer by four times with liquid nitrogen as the working fluid and by three-point-five times for the boiling of water. Das et al. [11] investigated the effect of SiO_2 nanomaterial coating and achieved an 80% increase in the HTC due to enhanced hydrophilicity and surface cavities. Goswami et al. [12] reported that the liquid evaporation rate was increased by contacting a subcooled liquid with an unsaturated gas stream in a cross-flow rotary packed bed to evaporate the volatile component. Thus, they determined that the water evaporation rate was more efficient than that of vertical thin film evaporators. Quan et al. [13] experimentally demonstrated that the mass transfer efficiency was improved by more than 8% with uniform heating compared to intensive heating. Li et al. [14] investigated a novel thermosiphon design that integrates fluidized bed heat transfer technology to enhance thermal performance. They found that the evaporation and condensation heat transfer coefficients could be improved by up to 8.9% and 50.9%, respectively. Jiang et al. [15] developed an experimental device to investigate heat transfer characteristics in a downflow circulating fluidized bed evaporator. Their findings revealed that the introduction of particles disrupted the laminar sublayer and increased the number of nucleation sites, resulting in a higher boiling heat transfer coefficient.

Both Euler–Euler and Euler–Lagrange models emerge as promising approaches for the numerical modeling of phase interface in boiling. While homogeneous phases are modeled by the Euler conservation equations in the Euler–Lagrange method, the vapor phase is tracked by the motion of individually moving spherical bubbles. On the other hand, the Euler–Euler method can handle any number of phases without major modifications in the formulation, which leads to accurate results for well-mixed or dispersed phases in engineering applications such as fluidized beds, bubble columns, and spray formation. It effectively models complex interactions such as drag, lift, and phase change using less computational resources than other methods that require explicit interface tracking. However, the lack of tracking sharp interfaces emerges as a drawback in explicit tracking of interfaces. Additionally, it relies on empirical or theoretical closure models to describe

phase interactions, which may produce uncertainty and complexity. To this end, the Euler–Euler approach is often used in conjunction with the volume of fluid (VOF) method based on the assumption that both phases share the same kinematic space. The vapor volume fraction is updated via the solution of a transport equation including the source term associated with mass transfer between liquid and vapor [12,16–18]. It uses a single set of momentum equations shared by the fluids and tracks the volume fraction of each phase within each computational cell across the domain. The VOF method accurately handles complex interface phenomena such as breaking waves, splashing, and droplet formation to satisfy mass conservation for each phase. Additionally, it provides a clear and accurate representation of the interface, which is critical in the visualization of bubbles [19–26]. Moreover, the application of open-source software in this context has been relatively rare [27–30]. In this study, the condensation of vapor bubbles in water is modeled using the VOF method within the OpenFOAM v2112 software, which facilitates the implementation of fields, equations, and operator discretization.

The innovative aspect of the present study is the development of a novel micro-baffle design aiming to control the formation of bubbles during film boiling and to increase heat transfer efficiency without any external intervention such as surface coating, contact crossflow packed beds, multi-stage flash, and fluidized bed. Unlike traditional heat transfer enhancement methods, this approach uniquely targets bubble dynamics at the microscale, offering a more direct and efficient means of optimizing heat transfer. In this context, an open-source computational fluid dynamics (CFD) model is employed to simulate bubble dynamics in film boiling. The accuracy of the numerical model is validated by comparing the results with existing experimental and numerical data in the literature. The validated model is then used to optimize the geometrical parameters of the proposed design and to maximize heat transfer performance based on thermal characteristics. The performance of the proposed design is evaluated according to various indicators. Numerical simulation results indicate that the proposed design can effectively modify bubble formation to meet specific objectives and provide a significant improvement in heat transfer performance.

2. Numerical Model and Setup

The interface between liquid and vapor phases is tracked by monitoring the volume fraction of each phase that varies between zero and one. A value of zero or one within a computational cell indicates that the cell is either completely empty or fully filled with a specific phase, respectively. The summation of volume fractions is always constant and equals to unity within a cell:

$$\alpha_v + \alpha_l = 1 \quad (1)$$

This ensures that the total volume of the cell is occupied by either vapor, liquid, or liquid-vapor phases. The interface between liquid and vapor phases can be tracked by solving the following transport equation for the vapor phase in the Volume of Fluid (VOF) method [31,32]:

$$\frac{\partial}{\partial t}(\rho_v \alpha_v) + \nabla \cdot (\rho_v \alpha_v u) = S_v \quad (2)$$

where α_v , ρ_v , and u represent the vapor volume fraction, density, and velocity field, respectively, and S_v denotes the mass source term associated with the phase change. The phase change is assumed to occur at a constant pressure and quasi-thermal equilibrium state in the Lee phase-change model [33]. Moreover, the phase change is mainly dependent on the deviation between interfacial cell temperature and saturation temperature. An empirical multiplier can be used to adjust associated mass flux through the interface. The mass transfer between phases can be defined as a mass source using the Lee model:

$$S_v = C \rho_l \alpha_l \left(\frac{T - T_{sat}}{T_{sat}} \right) \quad (3)$$

where C is the mass transfer intensity factor, ρ_l is the liquid density and α_l is the volume fraction of the liquid cell. Here, saturation and condensation processes can be modeled by shifting the sign of the C in Equation (3). The mass transfer intensity factor of 100 s^{-1} is considered an optimal value in the Lee phase-change model. Numerical results are highly sensitive to the intensity factor and values significantly higher or lower than 100 s^{-1} may result in unrealistic results [34–37]. A source term can be added to the right-hand side of momentum equations to account for virtual mass effects in two-phase flows [38,39]. In this study, we adopt the Lee phase-change model, which is integrated into a VOF framework to simulate mass transfer between liquid and vapor phases. The phase-change process is modeled by including a source term on the right-hand side of the continuity equation in VOF-based models that track the interface between phases [31,40–42].

Physical properties of the fluid can be calculated by a weighted averaging of volume fractions within a cell to reflect the phase mixture accurately:

$$\phi = \alpha_l \phi_l + \alpha_v \phi_v \quad (4)$$

where ϕ denotes the physical property of the mixture. Vapor and liquid phases share the same velocity field and can be governed by a single momentum equation [31]:

$$\frac{\partial}{\partial t}(\rho u) + \nabla \cdot (\rho u u) = -\nabla p + \nabla \cdot [\mu (\nabla u + \nabla u^T)] + \rho g + F_s \quad (5)$$

where p represents the pressure field, g is the gravitational acceleration vector and u is the mixture velocity. The body force F_s , resulting from the surface tension at the interface, can be calculated using the Continuum Surface Force (CSF) model [43]. The enthalpy at the phase change can be determined from the following equation:

$$\frac{\partial}{\partial t}(\rho E) + \nabla \cdot [u(\rho E + p)] = \nabla \cdot [k \nabla T] + S_h \quad (6)$$

where S_h is the volumetric energy source and E is the sensible enthalpy [31,32]:

$$E = C_p(T - T_{sat}) \quad (7)$$

Here, T is the temperature of the fluid and C_p is the specific heat capacity, which can be calculated from the following equation [31,32]:

$$C_p = \frac{\alpha_v \rho_v C_{p,v} + \alpha_l \rho_l C_{p,l}}{\alpha_v \rho_v + \alpha_l \rho_l} \quad (8)$$

where $C_{p,v}$ and $C_{p,l}$ are specific heat capacities of vapor and liquid phases, respectively.

The boiling heat flux generated from the solid to the fluid can be described by following Newton's law of cooling:

$$T_{boiling} = h(T_{sub} - T_{sat}) \quad (9)$$

where h is the heat transfer coefficient, T_{sub} and T_{sat} are subcooled and saturation temperatures, respectively.

The present study utilizes the icoReactingMultiphaseInterFoam solver in OpenFOAM v2112 for the simulation of phase-change heat transfer. Stability and accuracy of the numerical model are ensured through the Euler scheme for the implicit discretization of unsteady terms and Gauss-based schemes for the spatial discretization of convective and diffusive terms in the governing equations. The vanLeer scheme is adopted for the discretization of divergence terms in the multiphase interaction to improve the stability of the numerical model. Coefficients of a discretized equation are stored into a single matrix and each matrix is solved using a matrix solution algorithm in the segregated solution architecture of OpenFOAM v2112. In this study, the GAMG (Generalized Geometric-Algebraic MultiGrid) solver is employed for the pressure field and the smoothSolver is

used with the symGaussSeidel smoother for the remaining fields to ensure an efficient convergence. The Courant number is set to one to adjust the time step dynamically during the unsteady simulation of the film boiling process. The time step was calculated between 2.97×10^{-4} s and 1.2×10^{-3} s in the numerical simulations conducted in the present study.

As shown in Figure 1, a thin layer of vapor completely covers the surface of the heater by isolating liquid from the heater. Evaporation occurs at the interface, leading the generated vapor to continuously leave the film layer in the form of bubbles. The Rayleigh–Taylor instability, induced by the gravity at the liquid–vapor interface, results in a periodic wave pattern. The thickness of the vapor film can be predicted from the following equation [31]:

$$\delta = \frac{l_m}{64} \left(4 + \cos\left(\frac{2\pi x}{l_m}\right) \right) \quad (10)$$

where l_m is the critical wavelength:

$$l_m = 2\pi \sqrt{\frac{3\sigma}{(\rho_l - \rho_v)g}} \quad (11)$$

where σ is the surface tension coefficient and g is the gravitational acceleration. Dimensions of the rectangular domain are defined according to the critical wavelength.

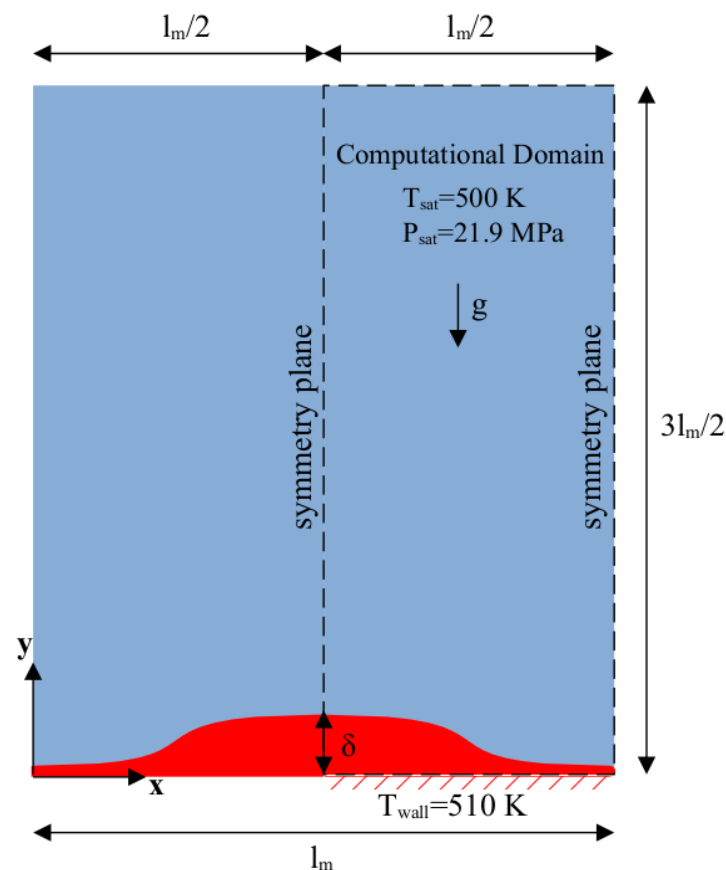


Figure 1. Schematic view of two-dimensional film boiling.

As shown in Figure 1, symmetry boundary conditions are applied at the vertical boundaries due to the fact that the numerical domain inherently exhibits horizontal symmetry. The heater surface at the lower boundary is modeled using a constant temperature boundary condition. The wall temperature is set to $T_{\text{sat}} + \Delta T$ [31,32,44], where ΔT is the temperature difference. A coded boundary condition is developed and implemented in the solver to generate the Taylor wavelength for the gas and liquid phases according to

Equation (10). Volume fractions of gas and liquid phases are set to one and zero, respectively, at the bottom wall. A no-slip boundary condition is imposed at the lower wall and a pressure-based velocity condition is applied at the upper wall. Pressure is set to zero and a zero gradient condition is used for the temperature and volume fraction at the upper boundary. A combination of Dirichlet and Neumann type boundary conditions ensures the stability and convergence of the present numerical model.

3. Results and Discussion

3.1. Validation of the Numerical Model

Two-dimensional film boiling illustrated in Figure 1 is considered for the validation of the numerical model. The initial temperatures of the liquid and interface are equal to the T_{sat} and the temperature of the vapor film layer varies linearly from $T_{sat} + \Delta T$ at the heater surface to the T_{sat} at the interface. The thermophysical properties of the fluid are given in Table 1, showing a saturation temperature of 500 K and a reference pressure of 21.9 MPa, which are both considered near critical conditions [31].

Table 1. Thermophysical properties of liquid and gas at near critical conditions.

Properties	Liquid	Gas
Density (kg/m^3)	$\rho_l = 200$	$\rho_g = 5$
Thermal conductivity (W/mK)	$k_l = 40$	$k_g = 1$
Thermal capacity (J/kgK)	$Cp_l = 400$	$Cp_g = 200$
Viscosity (Pa.s)	$\mu_l = 0.1$	$\mu_g = 0.005$
Surface tension (N/m)	$\sigma = 0.1$	-
Enthalpy of vaporization (J/kg)	$h_{lg} = 10^4$	-

Various mesh resolutions were generated and tested for $\Delta T_{sup} = 10$ K to achieve a mesh-independent solution. As compared with the numerical data from the literature in Figure 2, relatively coarse meshes exhibited premature bubble formation and separation, which is an indication of the importance of mesh resolution on the temporal and spatial variations of bubble formation. Identical bubble formations were captured, and the solution was no longer dependent on the mesh size when the mesh had 96×288 cells. The present mesh-independent solution is identical to the literature data. Therefore, this mesh could be used reliably in the remaining simulations.

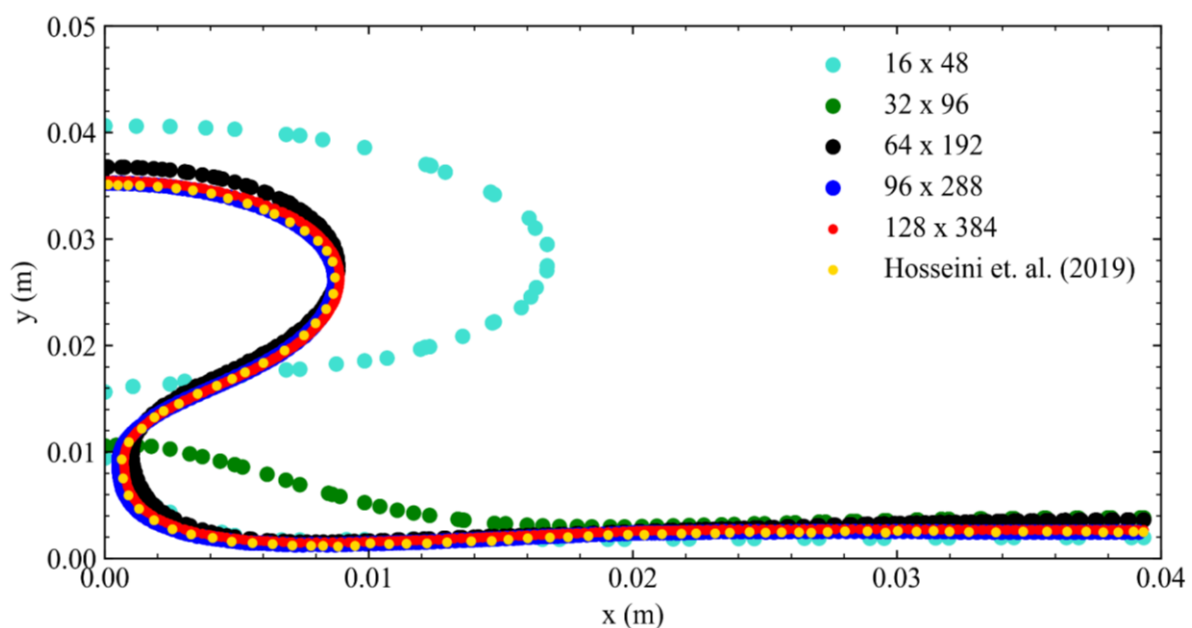


Figure 2. Bubble formations at $t = 0.85$ s using various mesh resolutions [31].

Two numerical simulations were performed using $\Delta T_{sup} = 10$ K and $\Delta T_{sup} = 30$ K and the results were compared with previously reported experimental and numerical results [31,44] in Figure 3. A good consistency was observed between present and previous results which indicates that the present numerical model can accurately capture the formation of bubbles under distinct heating conditions. As the temperature difference increases, the behavior of the separated vapor film switches from the quasi-periodic bubble regime to the jet column regime, which results in a long-term heat transfer. This observation proves that bubble formation is associated with heat transfer characteristics and can be managed by altering heat transfer at the interface.

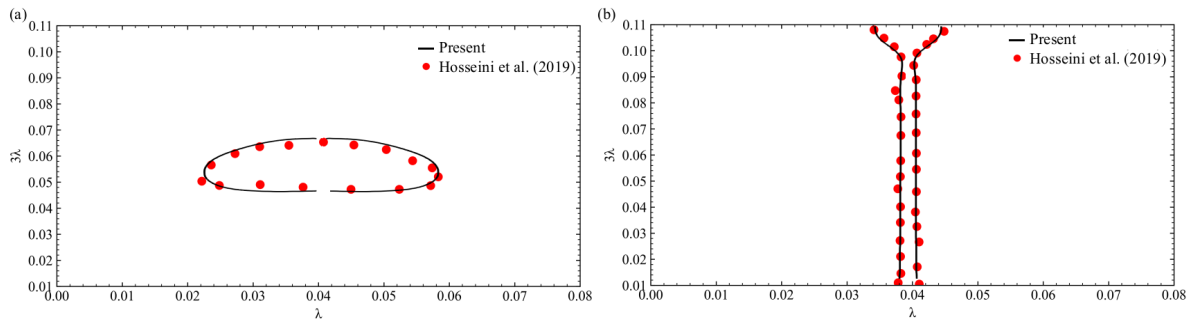


Figure 3. Comparison of vapor-liquid interface shapes [31] for (a) $\Delta T_{sup} = 10$ K and (b) $\Delta T_{sup} = 30$ K.

A function object is developed and implemented to the present numerical model for the calculation of the Nusselt number from the following equation:

$$Nu = \frac{\int_0^{l_m} \left(\frac{\lambda}{T_w - T_{sat}} \times \frac{\partial T}{\partial y} \right) \partial x}{l_m} \tag{12}$$

The Nusselt number was calculated and printed to an output file with a sampling period of 0.01 s during numerical simulation. Time variation of the calculated Nusselt number was compared with the results of Hosseini et al. [31] in Figure 4 along with the spatially averaged Nusselt numbers predicted by the Berenson and Klimenko correlation coefficients [45,46]. Figure 4 clearly proves that the present numerical model simulates evaporation-induced variation of the Nusselt number accurately. Thus, the present numerical model can be used reliably in the simulation-optimization of the micro-baffle design, which is discussed in the subsequent sections of the study.

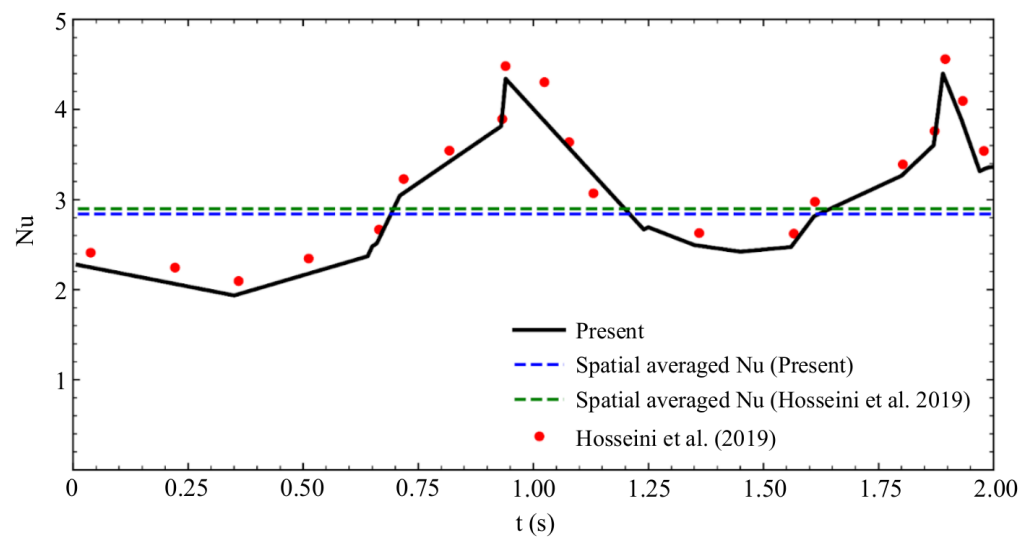


Figure 4. Comparison of time variation and spatially averaged Nusselt numbers [31].

3.2. The Micro-Baffle Design

The heat flux supplied from the bottom surface plays a vital role in the formation of bubbles. A continuous vapor layer forms on the bottom surface when the critical heat flux is exceeded, leading to a significant increase in surface temperature, which is essential for heat removal. Numerical simulations conducted in the present study pave the way to enhance heat transfer by altering flow and thermal fields. In this context, a micro-baffle that controls the formation of rising bubbles is proposed. As depicted in Figure 5, the baffle is placed at a specific location close to the heated surface and oriented from the bottom to the top with an angle of β . The location of the bottom corner of the baffle is represented by $C(x_b, y_b)$, the length of the baffle is L_b , and the orientation angle is β , all of which are design parameters to be optimized to achieve the best performance. The optimal location will be searched between minimum and maximum values of horizontal and vertical coordinates, which are calculated and listed in Table 2 for the present heating conditions. Values are also non-dimensionalized with respect to the wavelength to facilitate the interpretation of the design parameters in terms of wavelength.

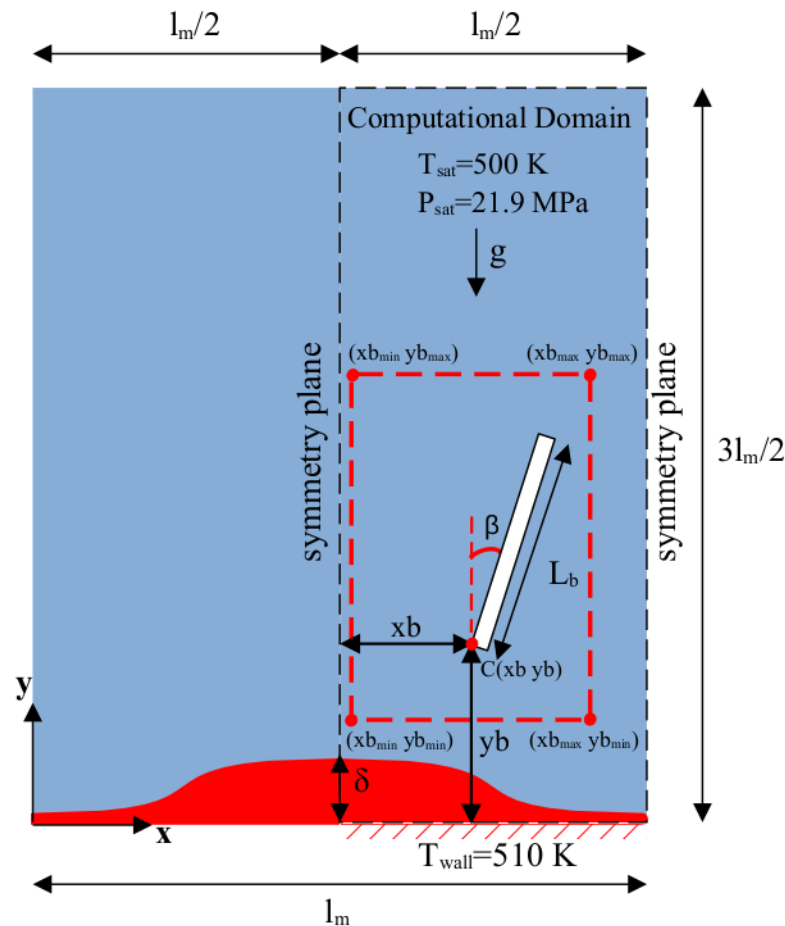


Figure 5. Parametric representation of the micro-baffle.

Table 2. Minimum and maximum coordinates of the baffle.

Variable	Value (mm)	Non-Dimensionalized with Respect to the l_m
$x_{b_{min}}$	5	1/16
$x_{b_{max}}$	20	1/4
$y_{b_{min}}$	5	1/16
$y_{b_{max}}$	15	3/16

3.3. Influence of the Baffle Location

Numerical simulations are performed by changing the location of the baffle corner at 2.5 mm and 5 mm in the horizontal and vertical directions, respectively, keeping $\beta = 0$ and $L_b = 20$ mm to see the influence of the location on the heat transfer characteristics. As listed in Table 3, minimum, maximum, and mean Nusselt numbers are calculated along with the performance improvement with respect to the no-baffle case, which is called Case₀. Maximum improvement has been achieved in Case_{xb3}, where $xb = 10$ mm and $yb = 5$ mm. Another important observation from the numerical simulations is that the influence of vertical coordinates is trivial on the heat transfer mechanism. Time variations of Nusselt numbers are plotted in Figure 6 for no-baffle and baffle cases. A significant improvement has been achieved in the Nusselt number when the location of the baffle has been optimized. The proposed design also reduced the period of the oscillating Nusselt number successfully. The Nusselt number also remains unchanged between the two peaks.

Table 3. Optimization of the baffle location.

Case	xb (mm)	yb (mm)	Nu_{min}	Nu_{max}	Nu_{mean}	Enhancement (%)
Case _{xb1}	5	5	2.9	4.2	3.6	13.5
Case _{xb2}	7.5	5	1.8	4.8	3.3	4.1
Case _{xb3}	10	5	3.8	5.9	4.8	53.6
Case _{xb4}	12.5	5	3.4	5.7	4.5	44.5
Case _{xb5}	15	5	3.1	5.6	4.3	37.5
Case _{xb6}	17.5	5	2.4	3.6	3.0	−5.9
Case _{xb7}	20	5	2.6	3.8	3.2	0.6
Case _{yb1}	10	7.5	3.6	5.9	4.8	50.8
Case _{yb2}	10	10	3.5	5.9	4.7	48.4
Case _{yb3}	10	12.5	2.5	4.3	3.4	47.9
Case _{yb4}	10	15	3.4	5.9	4.6	47.6

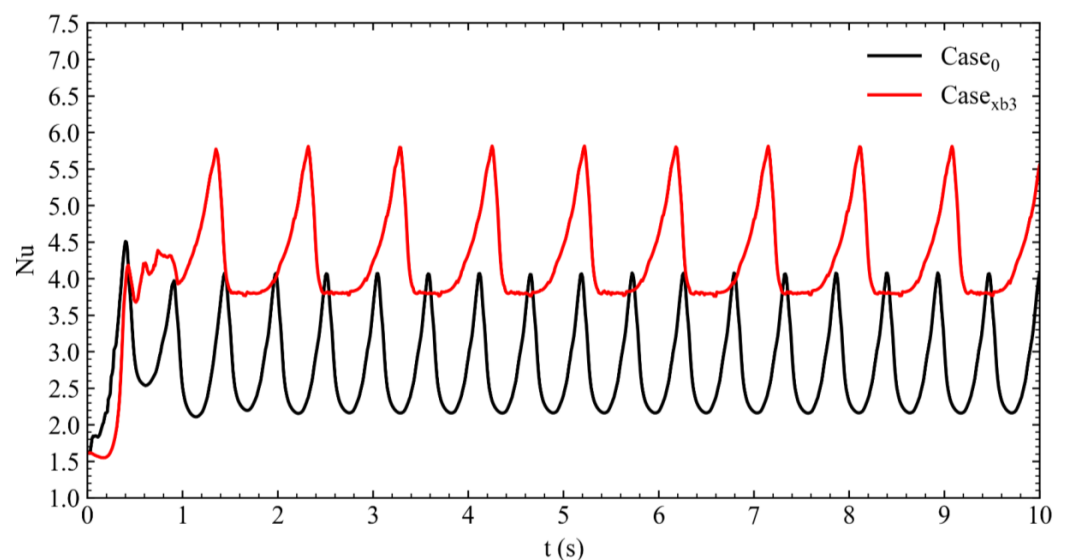


Figure 6. Time variations of the Nusselt numbers for Case₀ and Case_{xb3}.

3.4. Influence of the Baffle Length

The length of the baffle is crucial for the accumulation of gas within the channel and the continuity of the flow. The influence of the baffle length is investigated by changing the length of the baffle between 5 mm and 60 mm at the optimal location, determined in the previous part of the study. Maximum enhancement reaches 57.4% for $L_b = 40$ mm and the influence of the baffle length is observed to be trivial for longer baffles in Table 4. Thus, the optimal baffle length has been decided to be as $L_b = 40$ mm considering the cost of

the design, as the ratio of performance improvement to baffle length approaches zero. On the other hand, choosing a relatively smaller baffle length will provide flexibility in the implementation of the proposed design.

Table 4. Optimization of the baffle length.

Case	L_b (mm)	Nu_{min}	Nu_{max}	Nu_{mean}	Enhancement (%)
Case _{lb1}	5	1.6	4.8	3.2	0.9
Case _{lb2}	10	1.8	5.6	3.7	46.6
Case _{lb3}	15	3.8	5.8	4.8	52.8
Case _{lb4}	20	3.8	5.9	4.8	53.6
Case _{lb5}	25	3.8	5.9	4.9	54.2
Case _{lb6}	30	3.8	6.0	4.9	55.2
Case _{lb7}	35	3.8	6.0	4.9	55.8
Case _{lb8}	40	3.8	6.2	5.0	57.4
Case _{lb9}	45	3.8	6.2	5.0	57.5
Case _{lb10}	50	3.8	6.3	5.0	59.5
Case _{lb11}	55	3.8	6.3	5.0	59.6
Case _{lb12}	60	3.8	6.3	5.1	61.0

Time variations of the Nusselt numbers are compared in Figure 7 for Case₀ and Case_{lb8}. The proposed design has increased not only the Nusselt number but also the oscillation period by changing the formations of bubbles effectively. A strong interaction is observed between the oscillation period and the maximum value of the Nusselt number. Mean values are calculated when the quasi-steady-state is achieved.

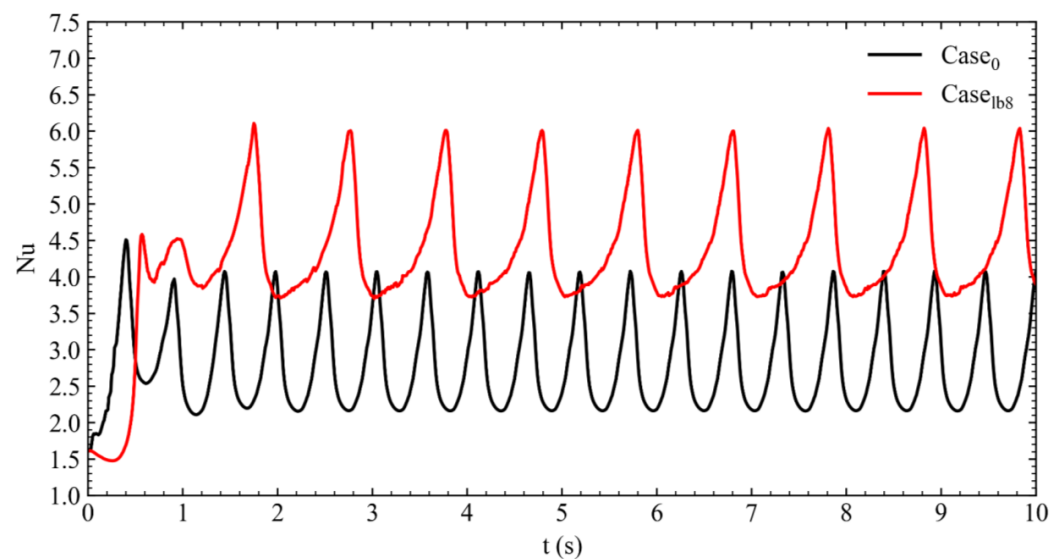


Figure 7. Time variations of the Nusselt numbers for Case₀ and Case_{lb8}.

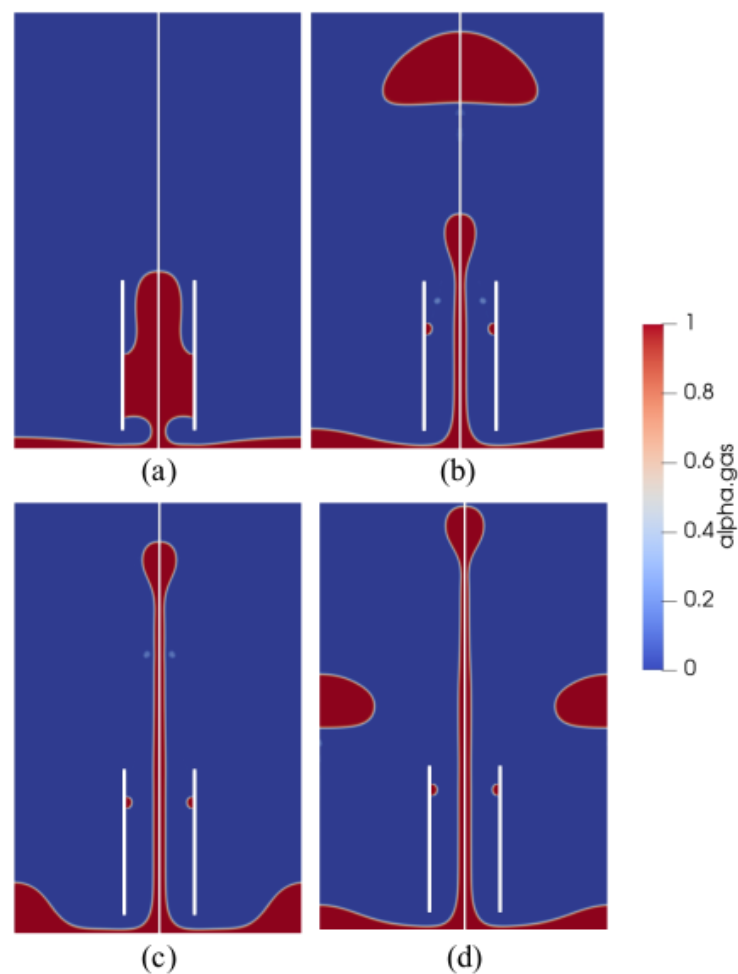
3.5. Influence of the Baffle Rotation

The effect of the orientation is investigated between 0° to 45° , keeping the baffle location and length as optimal values. The reason for choosing 45° as the upper limit is that it is the boundary angle where the baffle does not extend beyond the calculation domain. The baffle was oriented clockwise in the numerical experiments. Numerical simulation results listed in Table 5 revealed that the orientation angle has a negative effect on the Nusselt number due to the fact that the Nusselt number reduces once the baffle is oriented. Thus, the vertical baffle is preferred for maximum efficiency.

Table 5. Optimization of the baffle rotation.

Case	β (°)	Nu_{min}	Nu_{max}	Nu_{mean}	Enhancement (%)
Case $_{\beta 1}$	5	3.5	6.1	4.8	52.1
Case $_{\beta 2}$	10	3.2	5.9	4.6	45.5
Case $_{\beta 3}$	15	3.5	4.5	4	27.2
Case $_{\beta 4}$	20	3.7	4.6	4.1	31.6
Case $_{\beta 5}$	25	3.8	4.6	4.2	34.7
Case $_{\beta 6}$	30	3.8	4.5	4.2	32.6
Case $_{\beta 7}$	35	3.8	3.9	3.9	23.1
Case $_{\beta 8}$	40	2.5	3.1	2.7	−13.5
Case $_{\beta 9}$	45	2.3	2.6	2.5	−21.5

Formations of the bubbles are visualized for the optimal micro-baffle design in Figure 8. The optimal micro-baffle design has been observed to significantly increase the volume fraction of the gas phase just before the formation of the first bubble detaches from the lower surface. This elevated volume fraction leads to a rise in the Nu , which in turn enhances the heat transfer. The micro-baffle design creates larger and more continuous bubble formations that break apart over a longer duration. This modification reduces the period of the oscillating Nusselt number calculated on the bottom surface. Additionally, the optimal design promotes continuous bubble formation at lower temperatures. This continuous and stabilized bubble formation indicates a sustained increase in heat transfer efficiency as the process progresses.

**Figure 8.** Bubble formation for the optimal case at (a) $t = 0.71$ s (b) $t = 1.06$ s (c) $t = 1.55$ s (d) $t = 2.09$ s.

The CHF is a good indicator for the assessment of the heat transfer enhancement. The CHF is recognized as the maximum latent energy transport from the heating surfaces, which can be expressed as [47]:

$$q_{CHF} = u_c h_{lg} \rho_v \frac{A_g}{A_h} \quad (13)$$

$$u_c = \sqrt{\frac{2\pi\sigma}{\rho_v l_m}} \quad (14)$$

where u_c is the critical vapor velocity, h_{lg} is the latent heat of the working fluid, ρ_v is the vapor density, and A_g and A_h are areas of the vapor column and heater surface, respectively. The q_{CHF} values are calculated as 100.03 kW/m² and 166.40 kW/m² for the cases of no-baffle and optimal baffle design, respectively. Thus, the proposed design yields a 66.4% improvement in the CHF, which is a significant improvement.

4. Conclusions

This study explores the impact of a micro-baffle design on the bubble formation and heat transfer mechanism in film boiling through numerical simulations. An open-source numerical model was employed to simulate flow and thermal fields. The numerical model constitutes the Lee model for modeling phase-change induced momentum sources and the VOF method to capture bubble dynamics accurately. The numerical simulation results are found to be consistent with the previous experimental and numerical results.

A series of numerical simulations are performed for the optimization of the parameters of the proposed design. The results indicated that the vertical baffle yielded the maximum efficiency. While the horizontal position of the baffle significantly influenced the heat transfer performance, the vertical position was found to be less impactful. The length of the baffle emerged as a critical factor in enhancing heat transfer efficiency. The optimal baffle design resulted in a 57.4% improvement in the Nusselt number and a 66.4% increase in the CHF. Moreover, the proposed baffle facilitated the formation of a continuous bubble column, even with a smaller temperature difference between the wall and the subcooled liquid ($T_{wall} - T_{sub}$), which is essential for energy-efficient engineering designs where film boiling occurs.

The current study primarily focuses on the conceptual validation of a micro-baffle design for enhancing heat transfer during film boiling. The placement of the micro-baffles at the optimal location can be achieved using fine and high-temperature-resistant micro cables, which can be deployed laterally over the heat source. While the current approach demonstrates the feasibility of the design, future work will address practical considerations in more detail. This includes investigating the integration of the micro-baffle system in real-world settings, such as flow and pool boiling applications, where structural stability and ease of installation are critical.

Author Contributions: Conceptualization, O.M.S., M.K., S.Y. and E.D.; Methodology, O.M.S. and M.K.; Software, O.M.S., M.K., S.Y. and E.D.; Validation, O.M.S. and M.K.; Formal analysis, M.K. and E.D.; Investigation, M.K., S.Y. and E.D.; Data curation, O.M.S., M.K. and E.D.; Writing—original draft, O.M.S., M.K., S.Y. and E.D.; Writing—review and editing, E.D.; Visualization, O.M.S. and M.K.; Supervision, E.D.; Project administration, E.D. All authors have read and agreed to the published version of the manuscript.

Funding: This research is part of the HEATWISE project that has received funding from the European Union's Horizon Europe research and innovation programme under the Grant Agreement for Project No. 101138491 and the Swiss Secretariat for Education, Research, and Innovation (SERI) under contract No. 23.00606. Views and opinions expressed are, however, those of the author(s) only and do not necessarily reflect those of the European Union, CINEA, or SERI. Neither the European Union nor the granting authorities can be held responsible for them.

Data Availability Statement: The original contributions presented in the study are included in the article, further inquiries can be directed to the corresponding author.

Conflicts of Interest: Authors Onur Muhammed Sarikaya, Mustafa Kuzay, Sibel Yılmaz and Ender Demirel were employed by the company Design and Simulation Technologies Inc. The remaining authors declare that the research was conducted in the absence of any commercial or financial relationships that could be construed as a potential conflict of interest.

Nomenclature

A_g	Area of the vapor column (m ²)
A_h	Area of the heater surface (m ²)
α_v	Vapor volume fraction
α_l	Liquid volume fraction
δ	Knocker delta
μ	Dynamic viscosity (Pa.s)
ρ	Density (kg/m ³)
ρ_v	Vapor density (kg/m ³)
ρ_l	Liquid density (kg/m ³)
σ	Surface Tension (N/m)
C	Lee model constant
CHF	Critical Heat Flux
CFD	Computational Fluid Dynamics
CSF	Continuum Surface Force
C_p	Specific heat (J/kgK)
E	Sensible enthalpy
F_s	Body Force (Pa)
g	Gravity acceleration (m/s ²)
h	Heat transfer coefficient (W/m ² ·K)
h_{lg}	Latent heat (J/kg)
k	Thermal conductivity (W/mK)
l	Liquid volume
l_m	Critical wavelength
Nu	Nusselt number
p	Pressure (Pa)
q	Heat Flux (W/m ²)
S_h	Volumetric energy source
S_v	Mass source
T	Temperature (K)
T_s	Surface temperature (K)
T_{sat}	Saturation Temperature (K)
T_{sub}	Subcooled Temperature (K)
T_{sub}	Supply temperature (K)
T_{wall}	Wall Temperature (K)
u	Velocity field
u_c	Critical vapor velocity (m/s)
v	Vapor volume
w	Width (m)

References

1. Groeneveld, D.C.; Shan, J.Q.; Vasic, A.Z.; Leung, L.K.H.; Durmayaz, A.; Yang, J.; Cheng, S.C.; Tanase, A. The 2006 CHF look-up table. *Nucl. Eng. Des.* **2007**, *237*, 1909–1922. [[CrossRef](#)]
2. Tong, L.S.; Weisman, J. *Thermal Analysis of Pressurized Water Reactors*; American Nuclear Society: Westmont, IL, USA, 1979.
3. Totten, G.E.; Bates, C.E.; Clinton, N.A. Spray Quenching. In *Handbook of Quenchants and Quenching Technology*, 1st ed.; Haddad, M.T., Ed.; ASM International: Novelt, OH, USA, 1993. [[CrossRef](#)]
4. Faghri, A.; Zhang, Y. *Transport Phenomena in Multiphase Systems*, 1st ed.; Academic Press: Cambridge, MA, USA, 2006.
5. You, S.M.; Kim, J.H.; Kim, K.H. Effect of nanoparticles on critical heat flux of water in pool boiling heat transfer. *Appl. Phys. Lett.* **2003**, *83*, 3374–3376. [[CrossRef](#)]

6. Park, S.D.; Lee, S.W.; Kang, S.; Bang, I.C.; Kim, J.H.; Shin, H.S.; Lee, D.W.; Lee, D.W. Effects of nanofluids containing graphene/graphene-oxide nanosheets on critical heat flux. *Appl. Phys. Lett.* **2010**, *97*, 023103. [[CrossRef](#)]
7. Mori, S.; Okuyama, K. Enhancement of the critical heat flux in saturated pool boiling using honeycomb porous media. *Int. J. Multiph. Flow* **2009**, *35*, 946–951. [[CrossRef](#)]
8. Wang, K.; Gong, H.; Wang, L.; Erkan, N.; Okamoto, K. Effects of a porous honeycomb structure on critical heat flux in downward facing saturated pool boiling. *Appl. Therm. Eng.* **2020**, *170*, 115036. [[CrossRef](#)]
9. Hao, W.; Wang, T.; Jiang, Y.-Y.; Guo, C.; Guo, C.H. Pool boiling heat transfer on deformable structures made of shape-memory-alloys. *Int. J. Heat Mass Transf.* **2017**, *112*, 236–247. [[CrossRef](#)]
10. Surtaev, A.; Kuznetsov, D.; Serdyukov, V.; Pavlenko, A.; Kalita, V.; Komlev, D.; Ivannikov, A.; Radyuk, A. Structured capillary-porous coatings for enhancement of heat transfer at pool boiling. *Appl. Therm. Eng.* **2018**, *133*, 532–542. [[CrossRef](#)]
11. Das, S.; Saha, B.; Bhaumik, S. Experimental study of nucleate pool boiling heat transfer of water by surface functionalization with SiO₂ nanostructure. *Exp. Therm. Fluid Sci.* **2017**, *81*, 454–465. [[CrossRef](#)]
12. Goswami, N.; Basu, S.; Bhowal, A.; Datta, S. Concentration of solution in cross-flow rotating packed bed contactor. *Chem. Eng. Res. Des.* **2015**, *95*, 281–287. [[CrossRef](#)]
13. Quan, X.; Luo, Y.; Qie, S.; Huang, Z.; Liu, C. Mass transfer during falling film evaporation based on new multi-stage flash model. *J. Chem. Eng. Jpn.* **2015**, *48*, 528–532. [[CrossRef](#)]
14. Li, H.; Jiang, F.; Qi, G.; Li, X. Investigation of the thermal performance of a novel thermosyphon combined with fluidized bed heat transfer technology. *Powder Technol.* **2020**, *374*, 40–48. [[CrossRef](#)]
15. Jiang, F.; Feng, Q.; Qi, G.P.; Jiang, T.; Wang, J.J.; Liang, X.; Li, X.L. Flow boiling in a downflow circulating fluidized bed evaporator. *Appl. Therm. Eng.* **2019**, *156*, 359–370. [[CrossRef](#)]
16. Kunkelmann, C. Numerical Modeling and Investigation of Boiling Phenomena. Ph.D. Thesis, Technische Universität Darmstadt, Darmstadt, Germany, 2011.
17. Ginzburg, I.; Wittum, G. Two-phase flows on interface refined grids modeled with VOF, staggered finite volumes and spline interpolants. *J. Comput. Phys.* **2001**, *166*, 302–335. [[CrossRef](#)]
18. Hirt, C.W.; Nichols, B.D. Volume of fluid (VOF) method for the dynamics of free boundary. *J. Comput. Phys.* **1981**, *39*, 201–225. [[CrossRef](#)]
19. Yakubov, S.; Cankurt, B.; Maquil, T.; Schiller, P.; Abdel-Maksoud, M.; Rung, T. Euler-Euler and Euler-Lagrange approaches to cavitation modelling in marine applications. *CIMNE* **2011**, 544–555. [[CrossRef](#)]
20. Valizadeh, Z.; Shams, M. Numerical investigation of water-based nanofluid subcooled flow boiling by three-phase Euler–Euler, Euler–Lagrange approach. *Heat Mass Transf.* **2016**, *52*, 1501–1514. [[CrossRef](#)]
21. Butaye, E.; Toutant, A.; Mer, S. Euler–Euler Multi-Scale Simulations of Internal Boiling Flow with Conjugated Heat Transfer. *Appl. Mech.* **2023**, *4*, 191–209. [[CrossRef](#)]
22. Chen, M.; Liu, M.; Tang, Y. Comparison of Euler-Euler and Euler-Lagrange approaches for simulating gas-solid flows in a multiple-spouted bed. *Int. J. Chem. React. Eng.* **2019**, *17*, 20180254. [[CrossRef](#)]
23. Groll, R.; Jakirlić, S.; Tropea, C. Comparative study of Euler/Euler and Euler/Lagrange approaches simulating evaporation in a turbulent gas–liquid flow. *Int. J. Numer. Methods Fluids* **2009**, *59*, 873–906. [[CrossRef](#)]
24. Lou, W.; Zhu, M. Numerical simulation of gas and liquid two-phase flow in gas-stirred systems based on Euler–Euler approach. *Metall. Mater. Trans. B* **2013**, *44*, 1251–1263. [[CrossRef](#)]
25. Van Sint Annaland, M.; Deen, N.G.; Kuipers, J.A.M. Numerical simulation of gas bubbles behaviour using a three-dimensional volume of fluid method. *Chem. Eng. Sci.* **2005**, *60*, 2999–3011. [[CrossRef](#)]
26. Welch, S.W.; Wilson, J. A volume of fluid based method for fluid flows with phase change. *J. Comput. Phys.* **2000**, *160*, 662–682. [[CrossRef](#)]
27. Kleefsman, K.M.T.; Fekken, G.; Veldman, A.E.P.; Iwanowski, B.; Buchner, B. A volume-of-fluid based simulation method for wave impact problems. *J. Comput. Phys.* **2005**, *206*, 363–393. [[CrossRef](#)]
28. Zeng, Q.; Cai, J.; Yin, H.; Yang, X.; Watanabe, T. Numerical simulation of single bubble condensation in subcooled flow using OpenFOAM. *Prog. Nucl. Energy* **2015**, *83*, 336–346. [[CrossRef](#)]
29. Deshpande, S.S.; Anumolu, L.; Trujillo, M.F. Evaluating the performance of the two-phase flow solver interFoam. *Comput. Sci. Discov.* **2012**, *5*, 014016. [[CrossRef](#)]
30. Sun, D.L.; Xu, J.L.; Wang, L. Development of a vapor–liquid phase change model for volume-of-fluid method in FLUENT. *Int. Commun. Heat Mass Transf.* **2012**, *39*, 1101–1106. [[CrossRef](#)]
31. Hosseini, S.A.; Kouhikamali, R. A numerical investigation of various phase change models on simulation of saturated film boiling heat transfer. *Heat Transf.-Asian Res.* **2019**, *48*, 2577–2595. [[CrossRef](#)]
32. Samkhaniani, N.; Ansari, M.R. Numerical simulation of bubble condensation using CF-VOF. *Prog. Nucl. Energy* **2016**, *89*, 120–131. [[CrossRef](#)]
33. Lee, W.H. A pressure iteration scheme for two-phase flow modeling. In *Multiphase Transport Fundamentals, Reactor Safety, Applications*, 1st ed.; Veziroglu, T.N., Ed.; Hemisphere Publishing: Washington, DC, USA, 1980.
34. Chen, G.; Nie, T.; Yan, X. An explicit expression of the empirical factor in a widely used phase change model. *Int. J. Heat Mass Transf.* **2020**, *150*, 119279. [[CrossRef](#)]

35. Yang, Z.; Peng, X.F.; Ye, P. Numerical and experimental investigation of two phase flow during boiling in a coiled tube. *Int. J. Heat Mass Transf.* **2008**, *51*, 1003–1016. [[CrossRef](#)]
36. Fang, C.; David, M.; Rogacs, A.; Goodson, K. Volume of fluid simulation of boiling two-phase flow in a vapor-venting microchannel. *Front. Heat Mass Transf.* **2010**, *1*, 013002. [[CrossRef](#)]
37. Chen, S.; Yang, Z.; Duan, Y.; Chen, Y.; Wu, D. Simulation of condensation flow in a rectangular microchannel. *Chem. Eng. Process. Process Intensif.* **2014**, *76*, 60–69. [[CrossRef](#)]
38. Milne-Thomson, L.M. *Theoretical Hydrodynamics*, 5th ed.; Macmillan: London, UK, 1968; pp. 491–492.
39. Kendoush, A.A. The virtual mass of an oblate-ellipsoidal bubble. *Phys. Lett. A* **2007**, *366*, 253–255. [[CrossRef](#)]
40. Wang, J.; Li, Y.; Wang, L. Numerical study on pool film boiling of liquid hydrogen over horizontal cylinders. *Energies* **2022**, *15*, 1044. [[CrossRef](#)]
41. Hassani, M.; Kouhikamali, R. Heat and mass transfer modeling of R-245fa and R1233zd (E) with concurrent boiling and convective evaporation in falling film applications. *Int. J. Refrig.* **2020**, *117*, 181–189. [[CrossRef](#)]
42. Wang, J.; Li, Y.; Wang, L.; Xia, S.; Ren, J.; Mao, H.; Xu, Y. Numerical investigation on subcooled pool film boiling of liquid hydrogen in different gravities. *Int. J. Hydrogen Energy* **2021**, *46*, 2646–2657. [[CrossRef](#)]
43. Brackbill, J.U.; Kothe, D.B.; Zemach, C. A continuum method for modeling surface tension. *J. Comput. Phys.* **1992**, *100*, 335–354. [[CrossRef](#)]
44. Reimann, M.; Grigull, U. Free convection and film boiling heat transfer in the critical region of water and carbon dioxide. *Wärme-Stoffübertragung* **1975**, *8*, 229–239. [[CrossRef](#)]
45. Klimenko, V.V. Film boiling on a horizontal plate—New correlation. *Int. J. Heat Mass Transf.* **1981**, *24*, 69–79. [[CrossRef](#)]
46. Berenson, P. Film-boiling heat transfer from a horizontal surface. *J. Heat Transf.* **1961**, *83*, 351–356. [[CrossRef](#)]
47. Seo, H.; Bang, I.C. Revisiting the Rayleigh–Taylor instability and critical heat flux with R-123 for different heater sizes and pressures. *Int. J. Therm. Sci.* **2016**, *100*, 324–332. [[CrossRef](#)]

Disclaimer/Publisher’s Note: The statements, opinions and data contained in all publications are solely those of the individual author(s) and contributor(s) and not of MDPI and/or the editor(s). MDPI and/or the editor(s) disclaim responsibility for any injury to people or property resulting from any ideas, methods, instructions or products referred to in the content.